Open source simulation tool for electrophoretic stacking, focusing, and separation

Moran Bercovici[a], Sanjiva K. Lele[a,b], Juan G. Santiago[b,*]

[a] Department of Aeronautics and Astronautics, Stanford University, Stanford, CA 94305, USA
[b] Department of Mechanical Engineering, Stanford University, Stanford, CA 94305, USA

ARTICLE INFO

ABSTRACT

We present the development, formulation, and performance of a new simulation tool for electrophoretic preconcentration and separation processes such as capillary electrophoresis, isotachophoresis, and field amplified sample stacking. The code solves the one-dimensional transient advection-diffusion equations for multiple multivalent weak electrolytes (including ampholytes) and includes a model for pressure-driven flow and Taylor–Aris dispersion. The code uses a new approach for the discretization of the equations, consisting of a high resolution compact scheme which is combined with an adaptive grid algorithm. We show that this combination allows for accurate resolution of sharp concentration gradients at high electric fields, while at the same time significantly reducing the computational time. We demonstrate smooth, stable, and accurate solutions at current densities as high as 5000 A/m^2 using only 300 grid points, and a 75-fold reduction in computational time compared with equivalent uniform grid techniques. The code is available as an open source for free at http://microfluidics.stanford.edu.

© 2008 Elsevier B.V. All rights reserved.

1. Introduction

Electrophoretic preconcentration and separation techniques are well established and widely used in a variety of fields, including chemistry, biochemistry, pharmacology and genetics [1,2]. The interest in and utility of these techniques is evident from the large number of associated publications, now exceeding one paper per hour.[1] In concert with experiments, computer simulations offer a strong research tool for elucidating fundamental processes ruling the dynamics of electrokinetic separation and preconcentration methods. Such tools also offer the potential of greatly reducing experimental time and achievement of assays with optimal resolution and sensitivity. Despite significant progress in computational techniques, there remain many electrokinetic flow problems outside the capabilities of existing codes. This is especially true of electrophoresis processes involving high electric fields and ion density gradients and their coupling with chemical reactions. Examples of challenging electrokinetic problems include the effects of electromigration dispersion on capillary zone electrophoresis injections [4]; field amplified sample stacking (FASS)

with strong concentration gradients [5,6]; and isotachophoresis (ITP) assays with strong mobility differences and high current densities [7,8].

In 1986, Saville and Palusinski [9] formulated a convenient set of conservation equations for electrophoretic transport including multiple species in equilibrium with protons (for monovalent species only but including ampholytes). With some modifications and expansions on the work, the approach remains the standard method for formulating the dynamics of electrophoresis. The work by Bier et al. [10] in 1983 was the first published implementation of an electrophoresis code with this approach. A later publication in 1986 [11] presented the details of the numerical method. In addition to the discretized formulation of equation, it provided a time step stability criterion and an algebraic equation for equilibrium reactions. While the simulation showed good agreement with experiments and allowed new insight into physical mechanisms [12], it was limited, at that time, by numerical stability and resolution constraints to current densities of the order 40 A/m^2. Higher electric fields resulted in significant spurious oscillations, or required a large number of grid points leading to unacceptably long computational times. To reduce computation cost, Dose and Guiochon [13] proposed in 1991 a column segmentation algorithm in which computations were performed only in active regions of the domain where the derivatives are non-zero. While reporting significant improvement in computational time, the authors pointed out the complexity of the algorithm's book-keeping and the remaining difficulty in a priori choice of grid spacing. Ermakov

Table 1
Summary of the evolution of numerical codes for generalized electrokinetic transport. Emphasized are approaches taken toward handling high current densities (and associated high concentration and field gradients) and reducing computational time.

Authors	Year	Numerical scheme	Primary contribution(s)[a]
Bier et al. [10]	1983	Second order centered	First implementation of the electrophoretic code described in [9]
Saville and Palusinksi [9]	1986	Not applicable	Formulation of governing equations for multiple species including monovalent equilibria with protons
Palusinski et al. [11]	1986	Second order centered	Time step stability condition Algebraic equilibrium equations for monovalent ampholytes Demonstrated current densities of order $10\,A/m^2$
Mosher et al. [12]	1989	Second order centered	Model for protein mobility
Dose and Guiochon [13]	1991	Second order centered with column segmentation	Column segmentation Grid size condition for non-oscillatory solutions
Ermakov et al. [14]	1994	Second order centered with artificial dispersion	Higher resolution by use of artificial dispersion Demonstrated current densities of order $100\,A/m^2$
Mosher et al. [20]	1995	Second order centered	Model for electroosmotic flow
Martens et al. [15]	1997	Upwind with implicit time step	Demonstrated current densities of order $1000\,A/m^2$ Numerical dissipation leads to increased interface widths
Ikuta and Hirokawa [16]	1998	Shifted upwinding	Demonstrated current densities of order $1000\,A/m^2$ Numerical dissipation leads to increased interface widths
Sounart and Baygents [17]	2000	Flux-corrected transport (flux limiter)	Demonstrated current densities of order $1000\,A/m^2$ Reduced numerical dissipation Improved representation of interface widths
Breadmore et al. [19]	2006	Second order centered	Demonstrated current densities of order $10,000\,A/m^2$ using large grids
Hruska et al. [32]	2006	Second order centered	Accounts for ionic strength in activity coefficients and electric mobility Treatment of multivalent ampholytes Includes large database of analytes Free simulator available online
Yu et al. [18]	2008	Second order CESE	Demonstrated current densities of order $1000\,A/m^2$ Reduced numerical dissipation Improved representation of interface widths
Current work	2008	Sixth order compact scheme Adaptive grid	High resolution, sixth order scheme Adaptive grid Reduced computation time Demonstrated current densities of order $1000\,A/m^2$ with no numerical dissipation (accurate representation of sharp interfaces) Open source code

[a] Ionic current densities listed here are those reported in the original publications. Older numerical schemes listed are, of course, expected to allow the solution of significantly higher current densities on modern computers.

et al. [14], in 1994, were perhaps the first to recognize the importance of spatial discretization in reducing spurious oscillations. They achieved higher resolution by use of numerical dispersion and reported smooth solutions up to $100\,A/m^2$. While showing significant improvement over previous schemes, the limitation on electric field with the computers available at the time was still an order of magnitude lower than current densities used in the laboratory. In 1997, Martens et al. [15] and later Ikuta and Hirokawa [16] took a different approach by implementing upwind discretization. This upwinding allowed smooth solutions at current densities as high as $2200\,A/m^2$, but at the expense of introducing non-physical dissipation; this resulted in overly diffused (e.g., wider than known values from simple cases which are analytically solvable as will be discussed below) concentration interfaces. Significant improvements in the dissipative approach were offered by Sounart and Baygents [17] who proposed a flux-corrected transport method in which numerical dissipation is limited to grid points where it is required. Interface widths obtained with this method were significantly lower and closer to expected values, compared with upwind schemes. However, to achieve negligible numerical dissipation, the number of grid points (and thus the computational time) required by the flux-corrected transport method becomes equivalent to that required by second order centered schemes. Recently, Yu et al. [18] presented the use of the space-time conservation element and solution element (CESE) method for simulation

of electrophoresis problems at high current densities. Similar to the work by Sounart and Baygents, CESE offers limited numerical dissipation thereby improving the accuracy at interfaces compared with upwind schemes. With the improvement in computer power in both CPU speed and memory, larger grids with smaller grid spacing could be used. This enabled higher current density simulations to be obtained, using even the original second order centered scheme by Bier et al. [10]. Breadmore et al. [19], for example, reported in 2006 electrophoresis simulations using current densities higher than $20,000\,A/m^2$. However, further reduction in computational time is still much desirable to allow for the analysis of complex, high current density problems used regularly by experimentalists, and to allow for the construction of efficient optimization tools. While not intended to serve as a complete review of the field, Table 1 summarizes the evolution of electrophoresis solvers and highlights some of the primary contributions to electrophoretic simulations, with an emphasis on the numerical schemes used.

In the current work, we propose a new approach for spatial discretization of electrokinetic problems which achieves both high accuracy and low computational cost. As mentioned above, precise resolution of interface widths can be crucial for accurate simulation of modern applications. We therefore employed a sixth order compact scheme which is non-dissipative. More important than its high order is the high resolution of the scheme, allowing for the
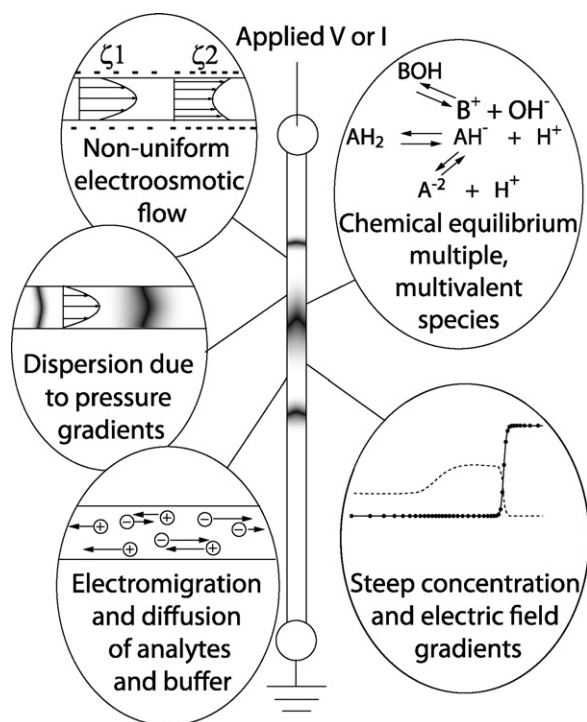
Fig. 1. Schematic illustration of an isotachophoresis process and physical mechanisms included in the current code. The code is a general solver for nonlinear electrophoresis of multiple, multivalent species. The code uses a high resolution adaptive grid scheme for reduced computational cost; this and a Taylor–Aris type dispersion model are unique to the code.

resolution of high wave numbers with fewer grid points. To further reduce the computational cost, and to provide a solution method which does not require an a priori choice of grid spacing, we developed an adaptive grid algorithm. The adaptive grid continuously varies the spacing of and clusters grid points in regions of high gradients, thereby reducing the possibility of numerical instability and oscillations. We achieve smooth and stable solutions at current densities as high as $5000 \, \text{A/m}^2$ using a number of grid points 50 times smaller than equivalent uniform grids which achieve the same resolution. We thereby reduce computational time by a factor of 75.

The physical modules implemented in our code include treatment of multi-species, multivalent equilibrium reactions (including multivalent ampholytes), non-uniform electroosmotic flow (see for example Mosher et al. [20], and Thormann et al. [21]), and pressure-driven flow. The latter are key to determining ion density gradients in electrokinetic flows with heterogeneous electrolytes [6,22]. For the first time, we include a Taylor–Aris dispersion [23–27] formulation with a multi-species, heterogeneous electrolyte flow solver. The main physical formulations (modules) included in the code are summarized in Fig. 1. The code also includes a graphical user interface and a database of over 300 analytes, based largely on the tables by Hirokawa et al. [28–31]. Currently, the code does not account for changes in reactivity and mobility due to ionic strength; but these important mechanisms will be incorporated in near-future improvements. While the code constitutes a rather general tool for CE, FASS, and ITP, among other assays, modern applications of electrophoretic simulations are wide and diverse and no single code can offer an answer to all applications. We therefore also offer the code as an open source, written in Matlab (The Mathworks, Natick, MA, USA). Our open source allows researchers to modify, add, remove, embed, or link part or all of the codes with additional components and other programs. The code is available for download at http://microfluidics.stanford.edu.

2. Conservation laws and governing equations

2.1. Equilibrium reactions

As noted by Saville and Palusinski [9], the kinetic rates for acid–base type reactions are typically slow compared with advection and diffusion rates in the system. We here adopt this approach and consider a system of analytes and buffer ions always in (proton and hydroxyl dissociation) chemical equilibrium throughout the channel. This approach allows much larger time steps to be used in the simulation, compared with those required to describe reaction kinetics. While we find that the vast majority of phenomena can be described with this simplification, slow reaction kinetics may in some cases have an important effect on separation assays, as shown by Gebauer and Bocek [33] and more recently by Khurana and Santiago [34].

Following the notation of Stedry et al. [35], the total concentration (i.e., analytical concentration) of a general ampholytes family i is given by

$$c_i = \sum_{z=n_i}^{p_i} c_{i,z}, \quad i = 1 \ldots N \tag{1}$$

where $c_{i,z}$ is the concentration of an ionic state of valence z belonging to the family i. We here define a "family" as all ionization states of a specie which associate or dissociate one or more protons (e.g., for histidine, the +2, +1, neutral, and −1 forms all constitute one family). n_i and p_i are the minimum and maximum valences of that family (respectively −1 and +2 for the histidine example), and N is the total number of specie families. The reaction between any two consecutive ionic states within one family are defined by an equilibrium coefficient of the form

$$K_{i,z} = \frac{c_{i,z} c_H}{c_{i,z+1}}, \tag{2}$$

where c_H denotes the concentration of hydronium ions, H^+. As shown by Stedry et al. [35], using Eq. (2) the concentration of each ionic state can be related to the concentration of the neutral state, $c_{i,0}$, and the hydronium concentration, c_H, by

$$c_{i,z} = c_{i,0} L_{i,z} c_H^z \quad z = n_i \ldots p_i \tag{3}$$

where

$$L_{i,z} = \begin{cases} \prod_{z'=z}^{-1} K_{i,z'} & z < 0 \\ 1 & z = 0 \\ \prod_{z'=0}^{z-1} K_{i,z'}^{-1} & z > 0 \end{cases} \tag{4}$$

Substituting Eq. (3) into Eq. (1) yields an important result relating the concentration of each ionic state within a family to the total concentration of that family

$$c_{i,z} = c_i \frac{L_{i,z} c_H^z}{\sum_{z=n_i}^{p_i} L_{i,z} c_H^z} \tag{5}$$

As discussed by Newman and Thomas-Alyea [36] and adapted for this case by Saville and Palusinski [9], the characteristic diffusion-advection length scales in the problem are significantly larger than the electric length scale (Debye length), justifying the use of the electroneutrality assumption. Using the notation above, this is explicitly expressed as

$$\sum_{i=1}^{N} \sum_{z=n_i}^{p_i} z c_{i,z} + c_H - c_{OH} = 0, \tag{6}$$

where c_{OH} is the concentration of hydroxyl. Using the equilibrium equation for water, $c_{OH}c_H = K_W$, an algebraic equation for c_H is obtained

$$\sum_{i=1}^{N} c_i \sum_{z=n_i}^{p_i} \frac{zL_{i,z}c_H^z}{\sum_{z'=n_i}^{p_i} L_{i,z}c_H^{z'}} + c_H - \frac{K_W}{c_H} = 0. \tag{7}$$

Here the total concentrations c_i are assumed to be known, as well as all the properties of the different species $L_{i,z}$. This equation is typically solved iteratively for each time step and each grid point in the simulation. Additional simplification of Eq. (7) is given in [37], where we derive a simple, more convenient polynomial form which can be written as

$$\sum_{i=1}^{N} c_i P_i + Q = 0, \tag{8}$$

where

$$Q = (x^2 - K_W) \prod_{j=1}^{N} \left(\sum_{z'=n_i}^{p_i} L_{j,z'} x^{z'-n_j} \right)$$

$$P_i = c_H \prod_{j=1}^{N} \left(\sum_{z'=n_j}^{p_j} L_{i,z'}(1 + (z'-1)\delta_{ij}) x^{z'-n_j} \right) \tag{9}$$

While the expressions for P_i and Q appear complex, they merely represent the coefficients of a polynomial, using the known quantities $L_{i,z}$. An important property of this new form of the net neutrality constraint problem is that the polynomials coefficients P_i and Q need to be calculated only for the first time step of the simulation, and these then hold for all spatial locations and subsequent times. Only the concentrations c_i change in time and space, as described in the next section. Other properties of this form, such as direct solution of the polynomial are discussed in [37].

2.2. Advection-diffusion equations

Following a derivation approach similar to that of Saville and Palusinski [9], we start from a set of area-averaged advection-diffusion equations for each ionic state within each family,

$$\frac{\partial c_{i,z}}{\partial t} = \frac{\partial}{\partial x} \left[\left(\mu_{i,z} \frac{\partial \phi}{\partial x} - u \right) c_{i,z} + D_{i,z} \frac{\partial c_{i,z}}{\partial x} \right] + R_{i,z}, \quad i = 1 \ldots N,$$

$$z = n_i \ldots p_i \tag{10}$$

Here $\mu_{i,z}$ is the ionic mobility, $D_{i,z}$ is the molecular diffusivity, ϕ is the electric potential, u is the advective velocity, and $R_{i,z}$ is the production rate. Since the net rate of production of the elementary species is zero (Saville and Palusinski [9]), summing Eq. (10) over all valences yields an equation which is independent of the production rates $R_{i,z}$,

$$\frac{\partial c_i}{\partial t} = \frac{\partial}{\partial x} \left[\frac{\partial (D_i c_i)}{\partial x} + \mu_i \frac{\partial \phi}{\partial x} c_i - u c_i \right] \quad i = 1 \ldots N, \tag{11}$$

where

$$\mu_i = \sum_{z=n_i}^{p_i} \mu_{i,z} g_{i,z}, \quad D_i = \sum_{z=n_i}^{p_i} D_{i,z} g_{i,z} \tag{12}$$

and

$$g_{i,z} = \frac{L_{i,z}c_H^z}{\sum_{z=n_i}^{p_i} L_{i,z}c_H^z}. \tag{13}$$

Chemical equilibrium is accounted for through the effective mobility, μ_i, and effective diffusivity D_i, which depend on local pH through the function $g_{i,z}$. The formulation above is our generalization of the formulation provided by Martens et al. [15]. The new, current formulation accounts for differences in diffusivity (if known) across ionic states, and provides a simplified, explicit expression for the degree of dissociation $g_{i,z}$. We note our formulation is therefore significantly different from that of Saville and Palusinski [9]. Most notably, the flux terms on the right hand side of Eq. (11) depend explicitly on the total concentration c_i, as opposed to a dependency on the individual $c_{i,z}$. Our approach has several advantages. First, it allows a clear definition of the effective mobility and diffusivity as a function of pH for the case of multivalent species. Second, it reduces the computational cost associated with multi-stage time integrators (such as the Runge-Kutta integrator, used in the this work): If the pH is assumed constant within each time step, the chemical equilibrium and resulting effective mobility can be calculated for the first stage of each time step, and then fixed for subsequent stages within the that time step. Thus values of c_i are updated several times during one time step, while μ_i and D_i are updated only once per time step. Sounart and Baygents [17] presented an alternative formulation that depends explicitly on the total concentration. However, their expressions of effective diffusivity contain the total concentration in the denominator, which may lead to singularity in regions where these concentrations vanish.

In Eq. (11), D_i can be regarded as the molecular diffusivity of the total concentration of specie i, c_i. This allows us to leverage an approximation of dispersion effects via a Taylor–Aris dispersion coefficient of the form

$$D_i^{eff} = D_i[1 + \beta \, Pe^2], \tag{14}$$

where $Pe = Ud/D_i$ is the Peclet number based on the dispersion velocity, U (the area-averaged velocity scale associated with internal pressure gradients), and the characteristic dimension of the channel cross section, d. β is a constant that depends on the shape cross section and can be calculated for arbitrary shapes (e.g., $\beta = 1/192$ for a circular cross section with diameter d), as shown by Dutta et al. [38]. We account for dispersion due to both externally imposed pressure gradients and internal pressure gradients arising from non-uniform electroosmotic flow (EOF). The dispersion velocity can be expressed as

$$U = \frac{d^2}{b\eta} \frac{\Delta P}{L} + (\overline{u_{EOF}} - u_{EOF}), \tag{15}$$

where ΔP is the external pressure gradient, L is the length of the channel, η is the kinematic viscosity, and b is a constant determined by the shape of the cross section ($b = 32$ for a circular cross section). u_{EOF} is the local electroosmotic velocity, and $\overline{u_{EOF}} = (1/L) \int_0^L u_{EOF}(x) \, dx$ is the axial-dimension averaged electroosmotic velocity in the channel. This assumes that internal pressure and electric field gradients vary only slowly along the channel axis [27]. This is certainly accurate for cases where electroosmotic flow is strongly suppressed and external pressure gradients are applied to the capillary (as we discuss in Section 4.4). In a future paper we will address the complex problem of dispersion in ITP regions with very high (fully three-dimensional) velocity gradients.

The electroosmotic velocity is currently based on the model by Mosher et al. [20] and does not take into account ionic strength effects as described by Thormann et al. [21]. At any location along the channel, the local electroosmotic mobility is calculated using the expression

$$\mu_{EOF} = g_{EOF} \mu_{EOF}^0 + (1 - g_{EOF}) \mu_{EOF}^c, \tag{16}$$

where μ_{EOF}^0 and μ_{EOF}^c are experimentally determined electroosmotic flow mobilities at two extreme pH conditions. g_{EOF} is the

dissociation level of the wall given by

$$g_{EOF} = \frac{10^{pH-pK_{a_W}}}{1 + 10^{pH-pK_{a_W}}}, \tag{17}$$

where pK_{a_W} is the (experimentally determined) equilibrium constant of the wall. The local electroosmotic velocity is then given simply by the product of the local EOF mobility and the local electric field, $\mu_{EOF} = \mu_{EOF}(d\phi/dx)$.

The advection-diffusion Eqs. (11) are coupled through the electric field $d\phi/dx$. An equation for the field can be derived by invoking current conservation, while accounting for both electromigration and diffusion currents. Advection currents are assumed negligible here. For a constant current density j, the electric field is given by

$$\frac{\partial \phi}{\partial x} = -\frac{1}{\sigma}\left(j + \frac{\partial S}{\partial x}\right), \tag{18}$$

where the conductivity and diffusive current are again expressed explicitly as a function of the total concentration and the local pH:

$$\sigma = \sum_{i=1}^{N} c_i \alpha_i, \quad \alpha_i = \sum_{z=n_i}^{p_i} g_{i,z} \mu_{i,z} Fz$$
$$S = \sum_{i=1}^{N} c_i \beta_i, \quad \beta_i = \sum_{z=n_i}^{p_i} g_{i,z} D_{i,z} Fz. \tag{19}$$

3. Numerical method

3.1. Spatial discretization

The majority of the numerical research in electrophoretic transport has been focused on dealing with numerical oscillations which arise from steep concentration gradients at high electric fields [13–18]. There have been two main approaches for dealing with this: non-dissipative and dissipative schemes. The non-dissipative approach uses a centered discretization for the spatial derivatives. Dose and Guiochon [13] showed that, for a second order centered scheme, the solution is guaranteed to be non-oscillatory if the Peclet number based on the grid size, $Pe_{\Delta x} = u\Delta x/D$, satisfies $Pe_{\Delta x} < 2$. Here u is total advection velocity, D is the diffusivity, and Δx is the grid spacing. As the electric field increases, smaller grid spacing is required to satisfy this requirement, leading to increased computational time.

The dissipative approach makes use of numerical dissipation terms to filter high frequencies that result in oscillation. Perhaps the most common dissipative scheme is the first order upwind scheme in which the first derivative of an arbitrary function $f(x)$ is given by

$$\frac{df}{dx} = \frac{f_j - f_{j-1}}{\Delta x} + O(\Delta x), \tag{20}$$

where the mesh nodes are indexed by j and f_j denotes $f(j\Delta x)$. This can be alternatively expressed as

$$\frac{df}{dx} = \frac{f_{j+1} - f_{j-1}}{2\Delta x} - \frac{1}{2}\Delta x\left(\frac{f_{j+1} - 2f_j + f_{j-1}}{\Delta x^2}\right). \tag{21}$$

The first term in Eq. (21) is a centered second order first derivative. The second term is the numerical dissipation term which has the form of a second order second derivative with a $\Delta x/2$ coefficient. This can be regarded as a diffusion term with a coefficient that depends on the grid spacing. This approach is attractive since a non-oscillatory solution is guaranteed, irrespective of the chosen grid spacing (the larger the grid spacing, the larger the numerical diffusion coefficient). However, in cases where the exact shape of concentration gradients is of interest, such as in ITP simulations, dissipative solutions are unsatisfying as they result in non-physical

(overly wide) concentration gradients. Although numerical dissipation can be reduced by decreasing the cell size, it will be small compared with molecular diffusion only when $(1/2)\Delta x < D/u$; precisely the requirement for the second order centered scheme to be non-oscillatory. Hence, for accurate solutions, dissipative schemes offer no benefit (we note that dissipative schemes may be useful for rough-yet-quick estimates). A comparison between an upwind and centered scheme for a realistic ITP case is provided in Section 4.1.

In the present work we adopt the non-dissipative approach, yet aim to avoid numerical oscillations and reduce computational time. For any discrete grid, there exists a maximum wave number (spatial frequency), k, that can be accurately represented on that grid. The Nyquist criterion sets an upper bound on this wave number, $k\Delta x < \pi$, where Δx is the grid spacing. If we regard the concentration distribution as a Fourier series consisting of waves at varying frequencies, then sharper gradients require higher wave numbers. For a fixed Δx, this obviously sets a limit on the maximum gradient that can be described. However, expressing derivatives on a discrete grid sets more restrictive limitations. As shown in the Fourier analysis by Lele [39], derivative operations result in dispersion of high wave numbers; i.e., these waves travel at a range of frequency-dependent velocities. This results in oscillations, since the different waves no longer combine to give the correct concentration profile. The spatial resolution of a scheme is determined by the range of wave numbers it can accurately resolve for a given grid. In this work, we use the sixth order tridiagonal compact scheme [18]. This scheme, while non-dissipative, has a much higher resolution compared to a second order scheme. For example, for the first derivative, the sixth order scheme resolves 70, 50 and 35% of the wave numbers to an accuracy of 10, 1 and 0.1%, respectively. This is compared to the standard second order centered scheme with resolving efficiencies of only 25, 8 and 2% of the wave numbers for the same accuracies.

In the compact scheme approximation, the finite difference approximation f_j' depends not only on the function values at surrounding nodes, but also on the derivative approximations at the neighboring nodes. This results in an implicit expression for derivatives. For the sixth order scheme employed here, the relation for the first derivative takes the form

$$\frac{1}{3}f_{j-1}' + f_j' + \frac{1}{3}f_{j+1}' = \frac{1}{9}\frac{f_{j+2} - f_{j-2}}{4\Delta x} + \frac{14}{9}\frac{f_{j+1} - f_{j-1}}{2\Delta x}. \tag{22}$$

Similarly, for the second derivative

$$\frac{2}{11}f_{j-1}'' + f_j'' + \frac{2}{11}f_{j+1}'' = \frac{3}{11}\frac{f_{j+2} - 2f_j + f_{j-2}}{4\Delta x^2} + \frac{12}{11}\frac{f_{j+1} - 2f_j + f_{j-1}}{\Delta x^2}. \tag{23}$$

When written for all grid points, these expressions result in tridiagonal systems which are solved at each time step. Additional information regarding the use of this compact scheme, its resolution and the corresponding boundary conditions can be found in [37].

3.2. Adaptive grid

To reduce the computational time of the code, while maintaining an accurate and non-oscillatory solution, we have developed an adaptive grid procedure. Given a fixed number of grid points in the domain, the adaptive procedure clusters grid point at regions of high gradient, at the expense of lower gradient regions. This method appears to be very well suited to CE and ITP type applications, where a considerable fraction of the channel remains largely undisturbed, while small, important regions experience high, propagating gradients.

The construction of the adaptive grid consists of two stages. In the first step, we formulate the finite difference derivatives on a general non-uniform grid. Second, we derive an equation which

governs the location of the grid points at all times. These steps are described further below.

We express the finite difference derivatives on the (physical) non-uniform grid in terms of a computational uniform grid. One way of achieving this is by defining a mapping function from the physical domain, which may have a non-uniform grid, to a computational domain which has a uniform grid (Spotz and Carey [40]). This mapping is defined as $x = x(z)$, where x is the physical domain and z is the computational domain. All spatial derivatives can now be recast as a function of z using the chain rule. For example $df/dx = (df/dz)(dz/dx)$, or in short notation $f_x = f_z z_x = f_z / x_z$. The derivatives f_z and x_z are with respect to the uniform grid z and therefore can be calculated using operation (22). Applying this procedure to Eq. (11) results in modified governing equations, expressed on the computational domain z, in which the coefficients of the different fluxes depend on the local grid density x_z

$$\frac{\partial c_i}{\partial t} = \frac{1}{x_z^2}\left[\frac{\partial^2(c_i D_i)}{\partial z^2} - \frac{\partial(c_i D_i)}{\partial z}\frac{x_{zz}}{x_z} + \mu_i c_i\left(\frac{\partial^2\phi}{\partial z^2} - \frac{x_{zz}}{x_z}\frac{\partial\phi}{\partial z}\right)\right.$$
$$\left. + \frac{\partial(\mu_i c_i)}{\partial z}\frac{\partial\phi}{\partial z}\right] + (x_t - u)\frac{\partial c_i}{\partial z}\frac{1}{x_z}, \tag{24}$$

with

$$\frac{\partial\phi}{\partial z} = -\frac{1}{\sigma}\left(j x_z + \frac{\partial S}{\partial z}\right) \tag{25}$$

and

$$\left(\frac{\partial^2\phi}{\partial z^2} - \frac{x_{zz}}{x_z}\frac{\partial\phi}{\partial z}\right) = -\frac{1}{\sigma}\left(\frac{\partial^2 S}{\partial z^2} - \frac{\partial S}{\partial z}\frac{x_{zz}}{x_z} + \frac{\partial\sigma}{\partial z}\frac{\partial\phi}{\partial z}\right). \tag{26}$$

To close the system, the mapping $x = x(z)$ has to be determined at each time step. To achieve this, we define an optimization problem in which the cost function takes maximum values at regions of high gradients. As shown in [37], the optimization problem can be recast as an additional PDE which governs the evolution of the mapping function $x(z)$,

$$\frac{\partial x}{\partial t} = -\lambda s(z), \tag{27}$$

where λ is a constant effecting the speed of propagation of the grid, and $s(z)$ is a smoothed form of the governing cost function, as described in [37]. This equation is solved coupled with the electromigration equations. Since regions of high gradients continuously migrate along the channel, the mapping function never reaches a steady state and areas of large grid density instead propagate with and accompany regions of high gradients.

3.3. Time discretization and simulation procedure

The code presented here is designed primarily to assist in the design and optimization of electrophoretic assays. For example, in CE, injection protocols, buffer selection, and detector placement have been shown to strongly influence resolution (Gas et al. [4], Bharadwaj et al. [41]); and in ITP the choice of electrolytes and electric field has been shown to play a key role in the stacking rate and maximum intensity of analytes (Enlund et al. [7] and Khurana and Santiago [22]). Accurate transient representation is essential in accommodating these needs.

Due to the coupled nature of the advection-diffusion equations, it is difficult to a priori determine a stable time step for the entire simulation. Furthermore, the adaptive time procedure may significantly alter the grid spacing during the simulation which directly affects the allowed time step. Automatic time step control has been therefore utilized in several previous publications. For example, Palusinski and coworkers [10] used the Runge-Kutta-Merson

and Ruge-Kutta-Fehlberg schemes, whereas Hruska et al. [32] used the Hamming predictor corrector scheme. In the current work, we adapted both the third order Runge-Kutta-Bogacki-Shampine (RK23) method and the fifth order Runge-Kutta-Dormand-Prince (RK45) method in the Matlab ODE suite [42]. These methods use two sequential Runge-Kutta orders to estimate the truncation error, and adjust the time step accordingly. The RK45 scheme is of higher order and allows for slightly larger time steps compared with the RK23 scheme. However, the latter requires less computational steps and was found to be faster, with negligible influence on accuracy. The RK23 method was therefore used for all simulations presented in this work. The simulation sequence can be summarized as follows:

(1) An initial distribution of total concentrations is defined by the user for all species along the channel.
(2) The initial grid distribution is automatically set to a uniform cell size.
(3) Net neutrality is satisfied by determining the local pH using the equilibrium Eq. (8).
(4) Using the obtained pH values, the effective mobility, effective diffusivity and electric conductivity are calculated for all species at all grid points using Eqs. (12) and (19).
(5) The cost function for the adaptive grid is calculated, and the right hand side of Eq. (27) is determined.
(6) All spatial derivatives required for the right hand side of the advection-diffusion Eq. (24) are calculated using the finite difference formulas Eqs. (22) and (23). Note that the time derivative of the grid mapping x_t (obtained in the previous step) is also required here.
(7) The governing equations for the species concentrations and the adaptive grid equations are integrated using the Runge Kutta integrator. The error norm is calculated, and this step is repeated until this norm meets a user specified tolerance. If the norm is significantly small compared to the tolerance, the time step is increased.
(8) New total concentrations are updated, and the process repeats from step three.

4. Results and discussion

As noted in Section 1, the code was implemented in Matlab to allow fast turn-around time in modifying, testing, and implementation of (new) physical modules, and to allow other researchers to modify it more conveniently. The results presented here were obtained using an un-complied version of the code under Matlab release version R2007b on a 32 bit Windows XP operating system. An Intel Core 2 Duo 2.0 GHz T7300 CPU with 2 GB of RAM was used as the computing platform (using only one of the cores). The computation times presented here should therefore only be used as a relative comparison among various schemes; since implementation in lower-level languages such as Fortran or C would significantly reduce the computational time associated with each.

4.1. Prediction of zone boundary thickness

We first investigate the influence of computational accuracy on zone boundary thickness in an example ITP assay. The mobility markers technique recently developed by Khurana and Santiago [44] leverages ITP for fluorescent detection of unlabeled analytes. Low concentration fluorescent marker zones bound analyte zones, so gaps in the fluorescent signal indicate the presence of analytes. A possible design goal for such assays is increasing their sensitivity by decreasing the amount (or concentration) of sample required for detection. In one of the experiments described in [44],

Table 2
Equilibrium constants and corresponding valences, fully ionized electrophoretic mobilities (at negligible ionic strength), and initial concentrations for analytes and mobility markers used in the numerical simulations of Fig. 2. Chemical properties for hydrochloric acid, Tris, acetic acid, fluorescein and 3-phenylpropionic acid are obtained from Hirokawa et al. [29] and Paul et al. [45]. The properties for tetraphenylborate, Oregon Green carboxylic acid and Bodipy are estimated from our own experimental observations.

Name	pK_a	Valences	Mobility ($\times 10^{-9}$ m^2 V^{-1} s^{-1})	Diffusivity ($\times 10^{-10}$ m^2/s)	Initial concentration
Hydrochloric acid (LE)	−2	−1, 0	−79.1	20.3	5 mM
Tetraphenylborate (TE)	5	−1, 0	−18	4.6	5 mM
Tris	8.076	0, +1	29.5	7.6	75 mM
Acetic acid (ACE)	4.756	−1, 0	−42.2	10.8	380 µM
3-Phenylpropionic acid (PPA)	4.664	−1, 0	−26.5	6.8	190 µM
Oregon Green carboxylic acid (M1)	4.7	−1, 0	−43	11.0	1.9 µM
Fluorescein (M2)	6.7, 4.4	−2, −1, 0	−33, −16.5	4.2	1.9 µM
Bodipy (M3)	5	−1, 0	−20	5.1	1.9 µM

the authors demonstrate the separation and detection of acetate (ACE) and phenylpropionate (PPA). We here simulate this separation and detection using the same chemistry, but with a lower initial concentration of the analytes. The leading electrolyte (LE) was composed of Tris–HCl and the terminating electrolyte (TE) was Tris–tetraphenylborate. A high TRIS concentration was used in both zones to yield an initial pH of 9.2. In the simulation the pH of the adjusted TE (i.e., the TE occupying regions formerly occupied by the LE) was 9.8. The chemical properties and initial concentrations as used in the simulation are provided in Table 2. The values of diffusivity here and throughout this work were calculated using the Nernst–Einstein relation $D_{i,z} = R_\mu T \mu_{i,z}/F$, where F is Faraday's constant, R_μ is the universal gas constant, and T is the temperature.

The simulation was performed twice: using an upwind scheme (e.g., as used in previous studies [15,17]), and using our sixth order compact scheme. In both cases an adaptive grid with 150 nodes was used at a current density of 289 A/m^2. The computational domain was 6 mm in length, and the problem was, in both cases, solved in a frame of reference moving with the plug. The analytes and markers were introduced as 1 mm plugs at the center of the channel.

Fig. 2 presents the simulation results for both schemes. The diffused boundaries obtained using the upwind scheme result in significant overlap between the markers and in lower maximum concentrations. In contrast, the sixth order compact scheme accurately resolves the interfaces showing three distinct marker peaks (below we verify the current scheme's accuracy by comparing it with a well-established analytical solution). For a fluorescent intensity proportional to the marker concentration, Fig. 2e and f represent the resulting signal. The dissipative scheme results in (non-physical) smearing of all three peaks, while our non-dissipative scheme clearly captures each peak.

We verify the accuracy of our numerical scheme by comparing to a simple test case where an analytical solution is available. In their appendix, Saville and Palusinski [9] discuss a three species ITP interface problem, where all species are fully ionized. The analytical solution for the ratio of LE to TE concentration in this case takes the form $c_{LE}/c_{TE} = \exp(-x/\delta)$, where x is the axial coordinate and

$$\delta = R_\mu T z_{LE} \left(\frac{\mu_{TE}(\mu_{LE} - \mu_{CI})}{\mu_{LE} - \mu_{TE}} \right) \frac{c_{LE}}{j} \qquad (28)$$

is the characteristic width of the interface. Here μ_{LE}, μ_{TE} and μ_{CI} are the mobilities of the LE, TE and counter-ion, respectively (signed values). z_{LE} is the valence of the LE, and j is the current density. A plot of this analytical solution for interface width is shown versus current density as the solid curve in Fig. 3. Results from our code are shown as circles. For these numerical solutions,
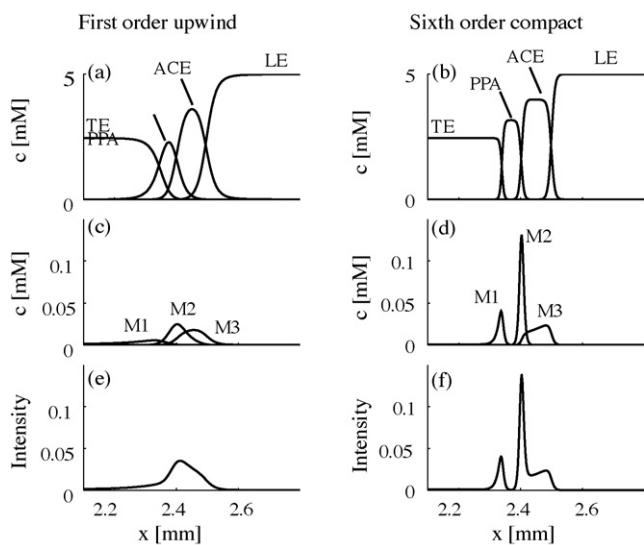

Fig. 2. Simulation results of separation and detection of acetate (ACE) and phenylpropionate (PPA) ions using three mobility markers. Chemical properties and initial concentrations used here are provided in Table 2. The left and right columns show respectively results obtained using the upwind and high resolution schemes. (a and b) Concentration profiles of non-fluorescent analyte zones and of LE, TE zones. The analytes zones are in plateau mode when using the non-dissipative scheme, but incorrectly appear to be in peak mode using the upwind scheme. (c and d) Concentration profiles of fluorescent mobility markers located at the interfaces between analytes. The marker species peaks are clearly resolved using the non-dissipative scheme, but significantly overlap using the upwind scheme. Here M$_1$: Oregon Green carboxylic acid, M$_2$: Fluorescein, and M$_3$: Bodipy. (e and f) The fluorescent signal for each assay. Analyte zone signals are merged on the left, and resolved on the right (current scheme).
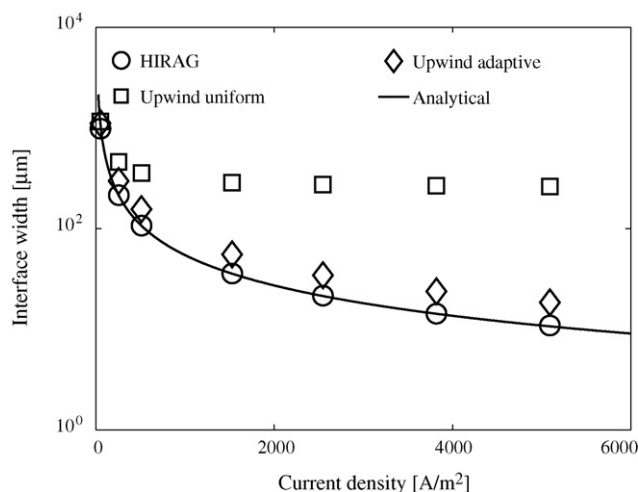

Fig. 3. Verification of the code's accuracy in resolving high gradient ITP interfaces. The analytical solution (solid line, available for the special case of three fully ionized species) is compared with numerical results (circles) obtained using the high resolution adaptive grid (HIRAG) with 100 grid points. HIRAG shows excellent agreement for the entire range of current densities (higher current densities are easily achieved using higher number of grid points). Results obtained using the upwind scheme, for the same number of grid points, show significant deviation from analytical values, even when combined with our adaptive grid.

the chemistry module was disabled and fully ionized mobilities of -60, -40 and $+50 \times 10^{-9}$ m^2 V^{-1} s^{-1} were assigned to the LE, TE and counter-ion, respectively (the same values used for the analytical expression). The computational domain was a 10 mm long capillary with a cross section diameter of 50 μm. 100 grid points were used to achieve a steady state solution by solving the problem in a frame of reference moving with the LE. Using the adaptive grid, this number of grid points allowed smooth solutions with current densities up to 5000 A/m^2. The solution at each current density was analyzed to extract the width of the interface. To be consistent with Eq. (28) the width is defined as the distance between the spatial coordinates corresponding to $c_{LE} = c_{TE}$ and $c_{LE}/c_{TE} = e^{-1}$. The numerical results (circles) show excellent agreement with the analytical solution (solid line).

For comparison, we also present in Fig. 3 numerical results obtained using the upwind (diffusive) scheme on both a uniform grid (e.g., similar to previous work [15,16]) and a non-uniform grid (using our current adaptive mesh module). As expected, the upwind scheme results in an overly diffused interface, with the uniform grid solution showing a deviation of nearly an order of magnitude from the analytical results. Our adaptive grid reduces this error, but the upwind still deviates significantly from the analytical curve at mid-range to high values of current density.

To test their numerical scheme, Ermakov et al. [14] defined several test cases. One was a cationic ITP simulation consisting of two analyte zones focused between a LE and a TE. The same test case was later adopted by Martens et al. [15] to show the dependency of the resulting boundary thickness on the choice of numerical scheme, and to test the stability of their algorithm at much higher current densities. Sounart and Baygents [17] again used this test case, at the same current density, to study the dependence of the zone boundary thickness on grid spacing. Yu et al. [18] recently used the same case to study the performance of their CESE scheme.

We here examine the test case examined by Ermakov, Martens, and others and compare the zone boundary thickness to the number of grid points used in the computational domain. These results are presented in Fig. 4. The LE was 18 mM sodium hydroxide ($\mu = 5.19 \times 10^{-9}$ m^2 V^{-1} s^{-1}), the TE was 40 mM β-alanine ($pK_a = 3.3$, $\mu = 36 \times 10^{-9}$ m^2 V^{-1} s^{-1}), and the background electrolyte was 20 mM acetic acid ($pK_a = 4.75$, $\mu = 4.24 \times 10^{-9}$ m^2 V^{-1} s^{-1}). Aniline ($pK_a = 4.8$, $\mu = 3.25 \times 10^{-8}$ m^2 V^{-1} s^{-1}) and pyridine ($pK_a = 5.16$, $\mu = 3 \times 10^{-8}$ m^2 V^{-1} s^{-1}) were introduced to the 40 mm long capillary as 1 mm long plugs at a concentration of 10 mM. The data for the UPWIND, PLPE1 and DIME schemes were digitized from Sounart and Baygents [17]. The data for the CESE scheme was obtained by calculating the width of the plug in the time domain and multiplying it by the ITP velocity [43]. The number of grid points used in those schemes was obtained by dividing the length of the channel by the specified (uniform) grid spacing. The dissipative schemes are characterized by a strong dependence on the number of grid points used. A higher grid density reduces the numerical dissipation and improves the accuracy of results.

In contrast to the other schemes, our high resolution adaptive grid (HIRAG) is non-dissipative so zone boundary is independent of the number of grid points. As with all non-dissipative schemes, significant numerical oscillations result if the grid density is not sufficiently high. However, for the test case, the zone boundary thickness was accurately resolved using the HIRAG scheme with 400 grid points, compared with more than 2500 required for the PLPE1 scheme. Further increase in the number of grid points did not change the HIRAG boundary thickness. Simulations using less than ∼400 grid points resulted in discernible numerical oscillations and their results are not presented here.

Overall, these data highlight the importance of accurately resolving zone boundaries, and that non-dissipative schemes can provide accurate, grid-size-independent solutions.
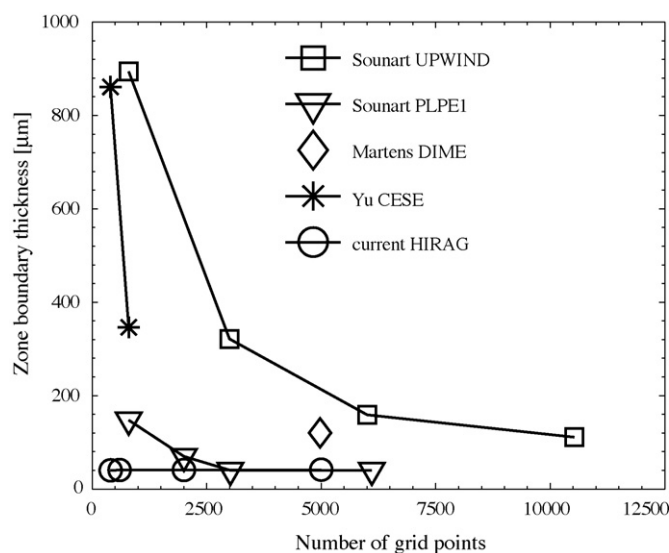

Fig. 4. The predicted thickness of the boundary between pyridine and aniline zones in ITP for various relevant computational schemes as a function of the number of grid points. Boundary thickness is defined here as the distance in which the concentration changes from 1 to 99% of its plateau value. Results are for a current density of 2260 A/m^2. The DIME and UPWIND schemes are highly dissipative and the interface width is grid-dependent even for a large number of grid points. The PLPE1 and CESE schemes exhibit reduced numerical dissipation and the PLPE1 scheme becomes independent of the grid after about 2500 grid points. The HIRAG scheme is non-dissipative and therefore, for non-oscillatory simulation conditions, is independent of the grid size.

4.2. Computational time

Here, we illustrate how our high resolution sixth order compact scheme combines with an adaptive grid (HIRAG) to reduce the total computational cost. We again take the (challenging) example of an ITP interface between an LE and a TE. To study the effect of the spatial discretization alone, the chemistry module is here disabled, and fully ionized monovalent LE, TE and counter-ion are used. The respective mobility values for these ions are -8×10^{-8}, -4×10^{-8} and $+1 \times 10^{-8}$ m^2 V^{-1} s^{-1}. Fig. 5 presents the simulation
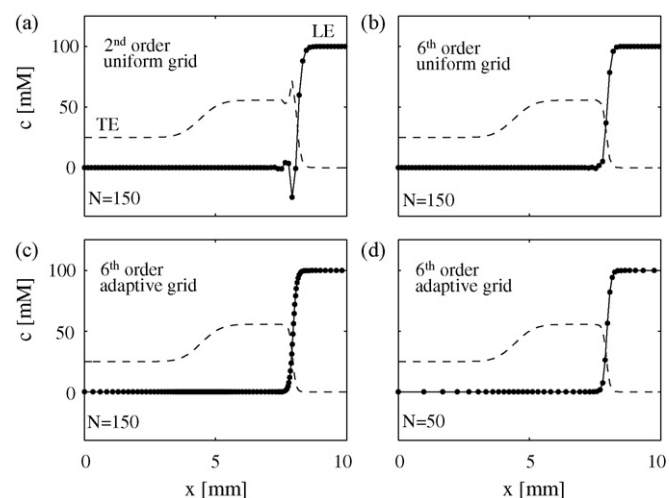

Fig. 5. Predicted concentration profiles showing the effect of spatial discretization and grid adaptation on the resolution of an ITP interface. N is the number of grid points used. Results obtained after 100 s on a 20 mm long domain, under a current density of 1800 A/m^2. For clarity, we here zoom in on a 10 mm length which captures the area of interest. (a) Explicit centered second order scheme using an equally spaced grid. (b) Sixth order compact scheme using an equally spaced grid. (c) Sixth order compact scheme using the adaptive grid procedure results in a smooth interface, (d) even for one-third the number of grid points.
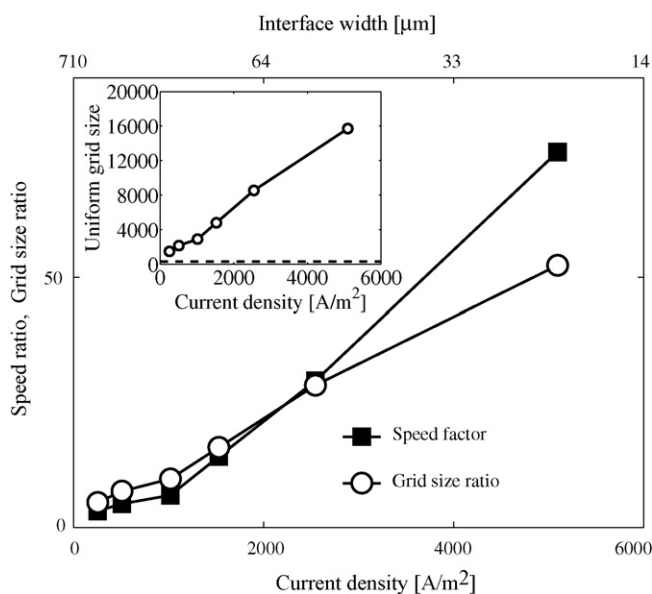
Interface width [μm]

Fig. 6. Speed ratio and grid size ratio associated with uniform and adaptive grid simulations of a single-interface ITP experiment. LE is 100 mM hydrochloric acid, TE is 50 mM HEPES, and counter-ion is 200 mM Tris. The channel is a 20 mm long circular capillary with a 50 μm diameter. Simulation time varied depending on the current density such that the distance traveled by the interface, $t/\mu_{LE}E_{LE}$, was constant. The curves are truncated at the maximum current resolvable by the 300 node adaptive grid. The inset shows the actual grid size used for the uniform grid (circles), compared to the constant 300 grid point value used by the HIRAG scheme (dashed line) to obtain the same resolution.

results using two schemes. The second order scheme is unable to resolve high wave numbers—resulting in significant oscillations. Using the same uniform grid, the sixth order compact scheme shows increased resolution and diminishes the magnitude and extent of oscillations. The sixth order scheme with an adaptive grid shows that oscillations are here completely eliminated, even when one third of the grid points are used (cf. bottom two plots of Fig. 5).

Next, we quantitatively evaluate the reduction in computational cost from using the adaptive grid. To this end, we compare the CPU time required to complete the same single-interface ITP simulation with and without the adaptive grid; and perform these comparisons as a function of applied current density. For each simulation, we analyzed output files to extract the minimum grid spacing (maximum grid density, which this occurred always at the LE–TE interface). This minimum grid spacing was then used in a uniform grid in a non-adaptive simulation; in this way, the interface resolution in both cases is approximately equal.

Fig. 6 presents both the grid size (number of grid points) ratio and the speed ratio as a function of current density. The speed ratio is defined as CPU time for the uniform grid solution divided by that of the adaptive grid solution. In both cases the sixth order compact scheme was used. As discussed by Saville and Palusinski [9], the interface width (and hence the local gradients) is inversely proportional to current density, but also directly proportional to the difference in mobilities of the two neighboring species. As a suitable, alternate-independent variable we therefore also show the associated interface width in the top axis of the figure. The LE was 100 mM hydrochloric acid ($\mu = 7.9 \times 10^{-8}$ m^2 V^{-1} s^{-1}), the TE was 50 mM 4-(2-hydroxyethyl)-1-piperazineethanesulfonic acid (HEPES) (pK_a = 7.5, $\mu = 2.35 \times 10^{-8}$ m^2 V^{-1} s^{-1}), and the counter-ion was 200 mM Tris (pK_a = 8.076, $\mu = 2.95 \times 10^{-8}$ m^2 V^{-1} s^{-1}). We use a very practical range of current densities [44,33]. For example, a 50 μm circular channel containing a buffer system consisting of 12 mM Tris base and 20 mM acetic acid, would result in a current density of ∼2500 A/m^2 under a 300 V/cm electric field. Current densities as high as 15,000 A/m^2 have been used in ITP [22].

Both speed ratio and grid size ratio are roughly proportional to current density as expected. At low to medium current densities, the speed ratio is slightly lower than the grid size ratio. We attribute this to the additional computational time dedicated to solving the adaptive grid equation. At current densities of approximately 2500 A/m^2 the speed ratio curve crosses that of grid size ratio. This speed gain is associated not with the number of grid points but with the time steps chosen by the Runge-Kutta integrator, as the stable time step is proportional to Δx^2. In the uniform grid case, the time step is therefore approximately constant throughout the simulation. However, the adaptive grid solution starts with much larger grid spacing, and develops small Δx values only as the interface steepens into its steady state form. This allows automatically for much larger time steps to be taken during the initial, low-gradient transients, resulting in an overall reduction in computational time. With our current (uncompiled) implementation in Matlab, the computational time for 5 s of simulated physical time at the highest current density presented (∼5000 A/m^2) were as follows: 1.2 min using the adaptive scheme (with 300 grid points) and 87 min using the uniform grid (with 15,709 grid points). As a comparison, we also used Simul 5 [32] (compiled) to solve the same case, using the same grid resolution (again, 15,709 nodes). The computation time was 41 min, with the maximum error set to 10^{-5}. We note that the computation time is generally faster with a higher allowed error (10^{-3} would yield acceptable results in most cases), yet for this case 10^{-5} was the highest value for which the code successfully completed 5 s of simulation time. The simulation settings using Simul 5 were as follows: ionic strength dependency disabled, EOF disabled, saving disabled, all refresh intervals set to 100 steps, and time step optimization enabled with an increment of 0.25 s. The channel length was set to 20 mm, with the injection site at 5 mm, a peak width of 1 mm, and peak edge width of 2 mm. Both walls were allowed to move with wall position initiation enabled, a wall refresh rate of 30 steps, and a wall increment of 100 nodes.

4.3. Capillary zone electrophoresis (CZE) of high concentration analytes

Another benchmark of interest originally set by Ermakov et al. [14] and later adopted by Sounart and Baygents [17] tests the ability of the numerical algorithms in describing CZE separation of high concentration analytes. Such conditions lead to strong coupling of the electric field and analytes concentrations. As a result, the analytes exhibit self-sharpening leading edges and tailing of trailing edges. Sounart and Baygents discuss in detail the results obtained under these conditions using a second order centered scheme, a first order upwind scheme and their proposed PLPE1 scheme. They investigate grid sizes of 400 and 2000 grid points and, for both of these, report large amplitude oscillations using the centered scheme and significant dissipation using the upwind scheme. The PLPE1 scheme was shown to yield more accurate results, but required a grid size of 2000 grid points for convergence (i.e., grid independence).

We here present simulation results using the HIRAG scheme with 400 grid points. The example is used to illustrate the behavior of the adaptive grid as regions of high gradients migrate along the channel. The background electrolyte was 12 mM Tris and 20 mM acetic acid. 1 mM of aniline (pK_a = 4.8, $\mu = 32.5 \times 10^{-9}$ m^2 V^{-1} s^{-1}) and pyridine (pK_a = 5.16, $\mu = 30 \times 10^{-9}$ m^2 V^{-1} s^{-1}) were introduced as 5 mm injection zones. A constant current of 5 μA was applied to the 50 μm diameter channel, equivalent to a current density of 2547 A/m^2. Fig. 7 presents the concentration profiles of the two analytes together with profiles of grid density. Details of the two analyte peaks are shown as three inset plots at the top of the figure (peaks are initially Gaussian and then triangular). The three main plots show grid density superposed on these peak profiles. At t = 0,
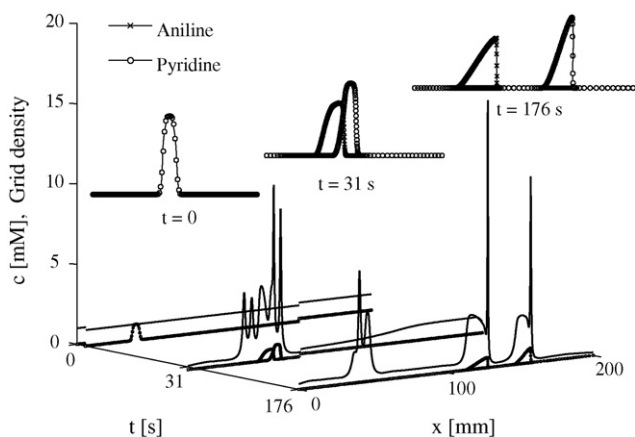
Fig. 7. Prediction showing the separation of aniline and pyridine in a 200 mm long channel using the HIRAG scheme with 400 grid points. At the top, are details of the analyte concentrations. High analyte concentrations (relative to background) result in nonlinear dynamics resulting in a sharp front and an electromigration dispersion tail. Grid density curves (thin black lines in main plots) indicate the ratio between the initial (uniform) grid spacing and the local grid spacing. The plot demonstrates how the adaptive grid recruits points from nearly constant (plateau) concentration regions and migrates these to regions of high gradients. A constant current of 5 μA was applied to the 50 μm diameter channel, equivalent to a current density of 2547 A/m².

the grid is uniform and grid density is a horizontal line. As electromigration develops, strong gradients build up and grid points accumulate in regions of such gradients. The highest two peaks in grid density occur at the sharp leading edges of the analytes (see largest two peaks at 31 and 176 s). As the analytes separate and migrate down the channel, high grid density regions continue to follow these sharp fronts, maintaining accuracy and eliminating oscillations. High grid densities persist in the injection region as expected due to the associated initial disturbance of the field and ion densities (this is a consequence of the initial local values of the Jovin and Alberty functions in these regions [46,47]). Other channel regions in which analytes have migrated (e.g., region near $x = 80$ mm at $t = 176$ s) return to low grid density values, efficiently distributing computational resources. The computational time for the latter case, using uncompiled Matlab, was 6.5 min for 240 s of physical time.

4.4. Taylor–Aris dispersion in CZE

We here summarize the effects of including Taylor–Aris dispersion on predictions of resolution, another unique feature of our code. Similar to the simulation in Section 4.3, we again investigate the separation of pyridine and aniline in an otherwise uniform buffer. Here the background electrolyte is 10 mM Tris and 40 mM acetic acid (pH 4.3). 1 mM of aniline and pyridine were introduced as a 1 mm injection zone. A constant current of 3 μA was applied to the 25 μm diameter channel, equivalent to a current density of 6110 A/m². Unlike the separation of Section 4.3, we now assume that an external pressure difference is applied to the channel to allow for more separation in a shorter physical separation distance (of 5 cm). The latter "counterflow" technique is commonly used in off- and on-chip electrophoretic separations [48,49]. The pressure gradient exactly balances the electromigration of pyridine. Thus, the total distance traveled by the analytes is proportional to their difference in (effective) mobility, roughly 10% of the mobilities magnitude. A potentially significant drawback of such a separation scheme is that the pressure gradient causes increased dispersion [41] which directly affects peak width and resolution.

Fig. 8 compares the separation resolution obtained for this case with and without the use of the Taylor–Aris dispersion model (cf. Eq.
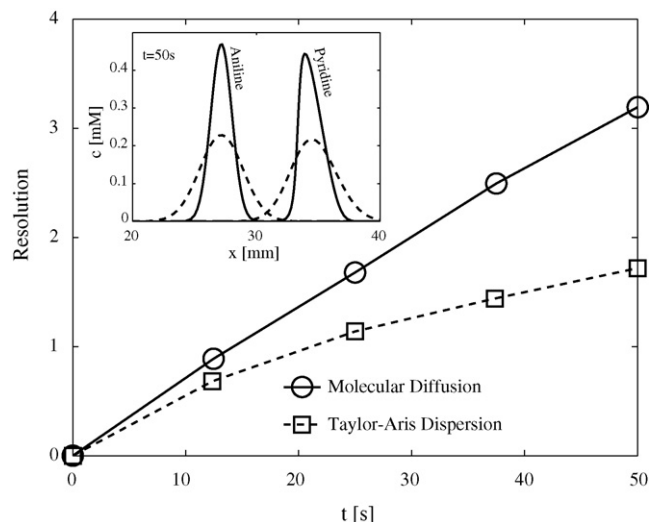

Fig. 8. Simulation of on-chip CZE separation of pyridine and aniline using a short (5 cm) channel, a current density of 6111 A/m², and an applied pressure gradient to balance electromigration. Modeling of molecular diffusion alone results in overly optimistic predictions of separation resolution and maximum concentration values. Application of the Taylor–Aris model accounts for the additional expected dispersion caused by the counterflow. The separation was simulated using the sixth order compact scheme with the adaptive grid using 200 grid points.

(14)). The resolution is defined here as $R = 2\Delta L/(w_1 + w_2)$, where $w_{1,2}$ are the widths (full width at half maximum) of the analytes peaks, and ΔL is the distance between them. Clearly, the use of a pressure gradient results in decreased resolution; decreasing R by approximately a factor of 2 after 50 s of separation. The inset to the figure shows a superposition of the analyte peak shapes at the end of the separation (with and without Taylor dispersion). Peak values are also decreased by a factor of 2 when dispersion is considered. Both resolution and signal-to-noise ratio of analyte peaks are major considerations in designing successful and optimal separations.

We verify our implementation of dispersion by comparing with the analytical expression for the shape of the sample zones, available for the case of linear advection-diffusion. In this weakly non-linear electrokinetic dispersion problem, the variance is expected to grow linearly in time so that $\sigma^2 = \sigma_0^2 + 2D_{eff}t$, where σ_0^2 is the initial sample zone width, D_{eff} is the effective diffusivity, and t is time [27]. A comparison between this dispersion theory (solid) and computational results is presented in Fig. 9. The two results are in good agreement, with small deviations at early times attributed to non-linearity associated with electromigration dispersion.

5. Conclusions and future work

We have demonstrated the implementation, performance and verification of a new numerical approach for the solution of non-linear advection-diffusion equations. We use a high resolution compact scheme, together with an adaptive grid (HIRAG) to achieve accurate solutions which are not contaminated by numerical dissipation. We have shown that such accuracy is important in challenging electrophoresis problems which require high resolution of steep concentration gradients such as isotachophoresis and electromigraiton dispersion in capillary electrophoresis. The HIRAG scheme also allows for the reduction in the number of grid points required for discretization and the subsequent reduction in computational time. For example, for an ITP simulation at moderately high current density (5000 A/m²), we have demonstrated a 75-fold reduction in computational time compared with an equivalent uniform grid solution. We have also demonstrated, for the first time,
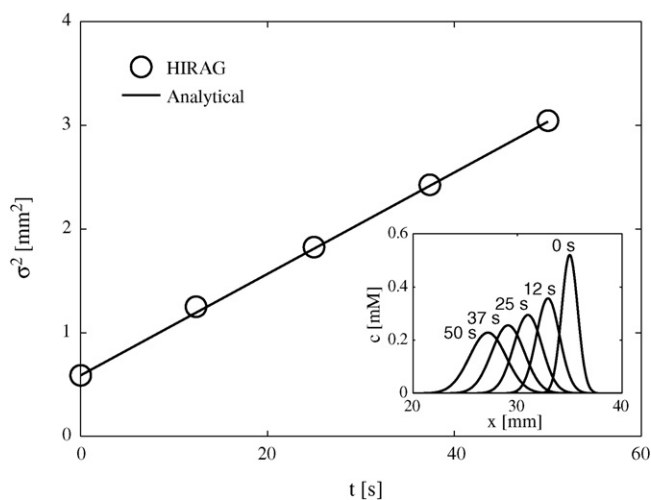
Fig. 9. Verification of numerical dispersion model (circles) using an analytical formulation for linear dispersion growth (solid line). For each time step, the concentration profile of the aniline (presented in the inset) is fitted to a Gaussian and the variance is extracted.

the incorporation of a Taylor–Aris dispersion model as an integral part of a one-dimensional numerical solver. Such a model is useful for more accurate predictions of electrophoretic assays which make use of pressure-driven flow, as well as for studying the effects of unwanted pressure gradients on resolution and signal intensity. Overall, the code is intended to assist researches and practioners in the design and optimization of electrophoretic processes, and is particularly well suited to preconcentration and separation assays. We offer the code as an open source so that other researchers may be able to modify it to fit their specific needs. It is available for free download at http://microfluidics.stanford.edu.

Our future work in this area will include incorporating the option of a dissipative scheme into our code, to provide a "rough approximation" type solution to many problems. As noted in the discussion, dissipative schemes typically result in overly diffused interfaces and are therefore less accurate in predicting properties such as resolution and sensitivity of assays. However, such schemes are very stable and can guarantee non-oscillatory solutions; making them very appropriate for quick estimates. Also, we will explore the use of our adaptive grid algorithm to mitigate the negative effects of increased dissipation. Future work will also include the incorporation of additional important physical models such as dependences of mobility and pK_a on ionic strength and other sources of dispersion.

References

[1] P.A. Auroux, D. Iossifidis, D.R. Reyes, A. Manz, Anal. Chem. 74 (2002) 2637.
[2] P.S. Dittrich, K. Tachikawa, A. Manz, Anal. Chem. 78 (2006) 3887.
[3] ISI Web of Science search engine, www.isiknowledge.com, Thomson ISI, Philadelphia, PA.
[4] B. Gas, P. Coufal, M. Jaros, J. Muzikar, I. Jelinek, J. Chromatogr., A 905 (2001) 269.
[5] D.M. Osbourn, D.J. Weiss, C.E. Lunte, Electrophoresis 21 (2000) 2768.
[6] R. Bharadwaj, J.G. Santiago, J. Fluid Mechanics 543 (2005) 57.
[7] A.M. Enlund, S. Schmidt, D. Westerlund, Electrophoresis 19 (1998) 707.
[8] B.G. Jung, Y.G. Zhu, J.G. Santiago, Anal. Chem. 79 (2007) 345.
[9] D.A. Saville, O.A. Palusinski, AIChE J. 32 (1986) 207.
[10] M. Bier, O.A. Palusinski, R.A. Mosher, D.A. Saville, Science 219 (1983) 1281.
[11] O.A. Palusinski, A. Graham, R.A. Mosher, M. Bier, D.A. Saville, AIChE J. 32 (1986) 215.
[12] R.A. Mosher, D. Dewey, W. Thormann, D.A. Saville, M. Bier, Anal. Chem. 61 (1989) 362.
[13] E.V. Dose, G.A. Guiochon, Anal. Chem. 63 (1991) 1063.
[14] S.V. Ermakov, M.S. Bello, P.G. Righetti, J. Chromatogr., A 661 (1994) 265.
[15] J. Martens, J.C. Reijenga, J. Boonkkamp, R.M.M. Mattheij, F.M. Everaerts, J. Chromatogr., A 772 (1997) 49.
[16] N. Ikuta, T. Hirokawa, J. Chromatogr., A 802 (1998) 49.
[17] T.L. Sounart, J.C. Baygents, J. Chromatogr., A 890 (2000) 321.
[18] J. Yu, Y. Chou, R. Yang, Electrophoresis 29 (2008) 1048.
[19] M.C. Breadmore, R.A. Mosher, W. Thormann, Anal. Chem. 78 (2006) 538.
[20] R.A. Mosher, C.X. Zhang, J. Caslavska, W. Thormann, J. Chromatogr., A 716 (1995) 17.
[21] W. Thormann, C.X. Zhang, J. Caslavska, P. Gebauer, R.A. Mosher, Anal. Chem. 70 (1998) 549.
[22] T.K. Khurana, J.G. Santiago, Anal. Chem. 80 (2008) 6300.
[23] G. Taylor, Proc. R. Soc. Lond. Ser A-Math. Phys. Sci. 219 (1953) 186.
[24] R. Aris, Proc. R. Soc. London Ser A-Math. Phys. Sci. 235 (1956) 67.
[25] H.A. Stone, H. Brenner, Ind. Eng. Chem. Res. 38 (1999) 851.
[26] H. Lin, B.D. Storey, J.G. Santiago, J. Fluid Mechanics 608 (2008) 43.
[27] R. Bharadwaj, D.E. Huber, T. Khurana, J.G. Santiago, in: J.P. Landers (Ed.), Handbook of Capillary and Microchip Electrophoresis and Associated Microtechniques, CRC Press, Boca Raton, FL, 2008, p. 1085.
[28] T. Hirokawa, T. Gojo, Y. Kiso, J. Chromatogr. 369 (1986) 59.
[29] T. Hirokawa, M. Nishino, Y. Kiso, J. Chromatogr. 252 (1982) 49.
[30] T. Hirokawa, Y. Kiso, B. Gas, I. Zuskova, J. Vacik, J. Chromatogr. 628 (1993) 283.
[31] T. Hirokawa, M. Nishino, N. Aoki, Y. Kiso, Y. Sawamoto, T. Yagi, J. Akiyama, J. Chromatogr. 271 (1983) D1.
[32] V. Hruska, M. Jaros, B. Gas, Electrophoresis 27 (2006) 984.
[33] P. Gebauer, P. Bocek, J. Chromatogr. 299 (1984) 321.
[34] T. Khurana, J.G. Santiago, LabChip, in press.
[35] M. Stedry, M. Jaros, V. Hruska, B. Gas, Electrophoresis 25 (2004) 3071.
[36] J.N. Newman, K.E. Thomas-Alyea, Electrochemical Systems, 3rd ed., Wiley-IEEE, Hoboken, NJ, 2004 (Ch. 11).
[37] M. Bercovici, S.K. Lele, J.G. Santiago, manuscript in preparation.
[38] D. Dutta, A. Ramachandran, D.T. Leighton, Microfluid. Nanofluid. 2 (2006) 275.
[39] S.K. Lele, J. Comput. Phys. 103 (1992) 16.
[40] W.F. Spotz, G.F. Carey, Int. J. Numerical Methods Heat Fluid Flow 8 (1998) 288.
[41] R. Bharadwaj, J.G. Santiago, B. Mohammadi, Electrophoresis 23 (2002) 2729.
[42] L.F. Shampine, M.W. Reichelt, Siam J. Sci. Comput. 18 (1997) 1.
[43] R. Yang, personal communication.
[44] T.K. Khurana, J.G. Santiago, Anal. Chem. 80 (2008) 279.
[45] P.H. Paul, M.G. Garguilo, D.J. Rakestraw, Anal. Chem. 70 (1998) 2459.
[46] T.M. Jovin, Biochemistry 12 (1973) 871.
[47] R.A. Alberty, J. Am. Chem. Soc. 72 (1950) 2361.
[48] C.T. Culbertson, J.W. Jorgenson, Anal. Chem. 66 (1994) 955.
[49] N.J. Reinhoud, U.R. Tjaden, J. Vandergreef, J. Chromatogr. 641 (1993) 155.